



**HAL**  
open science

## Convection in a vertical channel

Jean-Christophe Tisserand, Mathieu Creyssels, Mathieu Gibert, Bernard Castaing, Francesca Chillà

► **To cite this version:**

Jean-Christophe Tisserand, Mathieu Creyssels, Mathieu Gibert, Bernard Castaing, Francesca Chillà. Convection in a vertical channel. *New Journal of Physics*, 2010, 12, pp.075024. 10.1088/1367-2630/12/7/075024 . hal-00566067

**HAL Id: hal-00566067**

**<https://hal.science/hal-00566067>**

Submitted on 30 Nov 2011

**HAL** is a multi-disciplinary open access archive for the deposit and dissemination of scientific research documents, whether they are published or not. The documents may come from teaching and research institutions in France or abroad, or from public or private research centers.

L'archive ouverte pluridisciplinaire **HAL**, est destinée au dépôt et à la diffusion de documents scientifiques de niveau recherche, publiés ou non, émanant des établissements d'enseignement et de recherche français ou étrangers, des laboratoires publics ou privés.

## Convection in a vertical channel

This article has been downloaded from IOPscience. Please scroll down to see the full text article.

2010 New J. Phys. 12 075024

(<http://iopscience.iop.org/1367-2630/12/7/075024>)

View [the table of contents for this issue](#), or go to the [journal homepage](#) for more

### Download details:

IP Address: 156.18.40.173

The article was downloaded on 30/11/2011 at 13:47

Please note that [terms and conditions apply](#).

## Convection in a vertical channel

J-C Tisserand<sup>1</sup>, M Creyssels<sup>1,2</sup>, M Gibert<sup>1,3</sup>, B Castaing<sup>1</sup> and F Chilla<sup>1,4</sup>

<sup>1</sup> Université de Lyon, ENS Lyon, UMR 5672 CNRS, 46 Allée d'Italie, 69364 Lyon Cedex 7, France

<sup>2</sup> Ecole Centrale Lyon, LMFA CNRS, BP 163, 69131 Ecully Cedex, France

<sup>3</sup> MPI-DS (LFPN), Göttingen, Germany

E-mail: [Francesca.Chilla@ens-lyon.fr](mailto:Francesca.Chilla@ens-lyon.fr)

*New Journal of Physics* **12** (2010) 075024 (21pp)

Received 11 February 2010

Published 28 July 2010

Online at <http://www.njp.org/>

doi:10.1088/1367-2630/12/7/075024

**Abstract.** The flow generated by heat convection in a long, vertical channel is studied by means of particle imagery velocimetry techniques, with the help of the thermal measurements from a previous paper (Gibert *et al* 2009 *Phys. Fluids* **21** 035109). We analyse the mean velocity profiles and the Reynolds stresses, and compare the present results with the previous ones obtained in a larger cell and at a larger Reynolds number. We calculate the horizontal temperature profile and the related horizontal heat flux. The pertinence of effective turbulent diffusivity and viscosity is confirmed by the low value of the associated mixing length. We study the one-point and two-point statistics of both velocity components. We show how the concept of turbulent viscosity explains the relations between the local probability density functions (pdf) of fluctuations for temperature, vertical and horizontal velocity components. Despite the low Reynolds number values explored, some conclusions can be drawn about the small scale velocity differences and the related energy cascade.

<sup>4</sup> Author to whom any correspondence should be addressed.

**Contents**

<b>1. Introduction</b>	<b>2</b>
<b>2. Experimental setup</b>	<b>4</b>
<b>3. Brief overview of thermal results</b>	<b>5</b>
<b>4. Mean transverse profiles</b>	<b>6</b>
<b>5. Mean flow discussion</b>	<b>11</b>
<b>6. One-point statistics</b>	<b>13</b>
<b>7. Two-point statistics</b>	<b>15</b>
<b>8. Conclusions</b>	<b>19</b>
<b>Acknowledgments</b>	<b>20</b>
<b>References</b>	<b>20</b>

**1. Introduction**

Free convection in a long vertical channel is particularly well designed for modelling natural convection, such as that occurring in stars, in a planet's atmosphere or in half-natural situations, such as industrial plants. It allows the study of mixing phenomena in the bulk of the fluid, far from scalar injecting boundaries, with a minimum number of control parameters. The first one is the Prandtl number  $Pr = \nu/\kappa$ , where  $\nu$  is the kinematic viscosity and  $\kappa$  the heat diffusivity. The second control parameter is the Rayleigh number,

$$Ra = \frac{g\alpha\beta L^4}{\nu\kappa}, \quad (1)$$

where  $g$  is the gravitational acceleration and  $\alpha$  the constant pressure thermal expansion coefficient.  $\beta$  and  $L$  deserve a wider explanation.

Let us choose the origin of the temperature  $T$  such that its time and space average, on the whole channel, is zero.  $\langle T \rangle$  is the time-averaged temperature and  $\beta = -d\langle T \rangle/dz$  is the temperature gradient that drives the flow. If the thermal expansion coefficient  $\alpha > 0$ , which is the general case, convection occurs if the hot fluid is below the cold one ( $\beta > 0$ ).

$L$  is a characteristic length of the flow. The natural choice is  $d$ , the width of the channel. In a recent paper [1], thermal measurements yield another choice for  $L$ . We shall come back to this point later.

For experimental realizations, the considered channel connects two chambers, the hot one at the bottom and the cold one at the top. The sketch of such an experiment is shown in figure 1.

Note that salted water has been used for a similar study. For instance, the authors of [2]–[4] looked at the free convection in a vertical tube connecting two chambers with different salt concentrations. They studied a flux of salt instead of a flux of heat, and the salt diffusion coefficient (respectively the Schmidt number  $Sc$ ) takes the place of  $\kappa$  (respectively  $Pr$ ). Some numerical simulations [5, 6] also correspond well to this situation, using periodic boundary conditions.

As in the Rayleigh–Bénard case (the other great paradigm in thermal convection), the state of the system can be characterized by its global response to the above applied parameters.

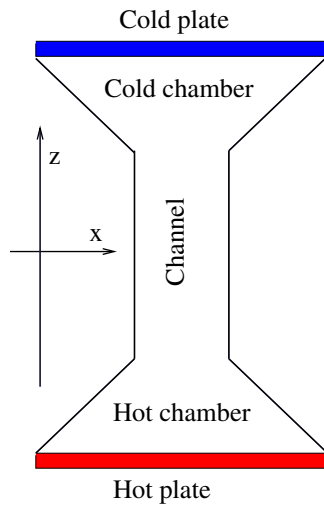


**Figure 1.** Sketch of the cell arrangement.

For instance, the Nusselt number ( $Nu$ ) compares the global heat flux to a purely diffusive one,

$$Nu = \frac{Q}{\chi\beta}, \quad (2)$$

where  $Q$  is the heat flux across the channel and  $\chi$  is the heat conductivity of the fluid. One can also define a Reynolds number

$$Re = \frac{UL}{\nu}, \quad (3)$$

where  $U$  is a typical velocity, which can be determined in various ways, indirectly through thermal measurements or directly through particle imagery velocimetry (PIV) techniques.

We can now come back to the choice of the characteristic length  $L$ . In [1, 7], it was noted that results appeared clearer when  $L$  was chosen as the ratio between a typical amplitude of temperature fluctuations  $\theta$  and the gradient  $\beta$ . With such a definition,  $L/d$  was observed to be constant for  $Re$  being smaller than some threshold value, and increased regularly above this threshold, apparently linear with  $\ln Re$ . The measurements made with the cell described in section 2 all correspond to Reynolds numbers lower than the threshold, where  $L/d$  can be considered as constant.

However, global measurements are not the only information that can be extracted from this system. PIV measurements allow a rather complete knowledge of the flow, which proves to be much simpler than in a Rayleigh–Bénard cell [8]. In a Rayleigh–Bénard cell, the flow is very inhomogeneous, the neighbourhood of plates, that of walls, the centre of the cell and the corners all corresponding to different statistical properties. Here, the turbulent flow is rather homogeneous, presenting translational invariance along the  $z$ -axis, and constant mean profiles, both of temperature and velocity, can be defined.

The paper is organized as follows. In section 2, the experimental setup and experimental procedures are exposed. In section 3, the results of thermal measurements are recalled, with reference to the corresponding papers. We then come to the new PIV measurements, with the mean profiles (section 4), and we discuss their implications (section 5). The following two

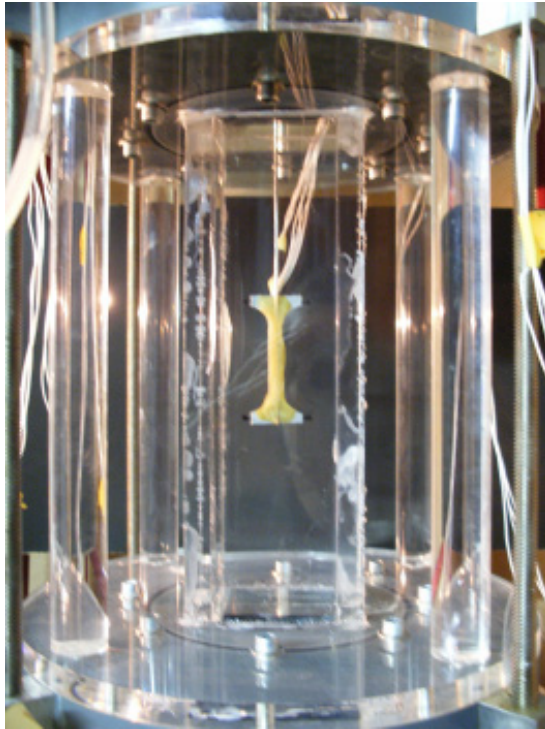


**Figure 2.** Picture of the cell. The ‘I’ structure (the bridge) measuring the vertical temperature gradient is visible in the middle of the channel.

sections are dedicated to the characterization of the produced turbulence, both with one-point (section 6) and two-point (section 7) statistics. We then conclude in section 8.

## 2. Experimental setup

Our cell, sketched in figure 1 and shown in figure 2, is filled with water. The chambers are conical and axisymmetric: the upper one is cold and the other is hot. As one can see in figures 1 and 2, these two chambers are linked through a square channel, 20 cm in length and  $5 \times 5 \text{ cm}^2$  in cross-sectional area. The walls of the channel, 10 mm thick, are made of polymethylmethacrylate (PMMA). A regulated water bath controls the temperature of the upper plate. The hot chamber is closed with a bottom plate that is heated by the Joule effect, thanks to a heating wire. With a power supply, the power provided to the water varies between 3 and 80 W, which allows the Rayleigh number to be in the range between  $4 \times 10^5$  and  $4 \times 10^6$ .

For vertical temperature gradient measurements in the channel, we use a bridge with four thermistors, from the same batch. The typical values of resistance are  $2 \text{ k}\Omega$  at  $20^\circ\text{C}$  and  $1 \text{ k}\Omega$  at  $40^\circ\text{C}$ . These sensors are welded at the corners of a rectangle, the width of which is 2.5 cm and the height of which is 5 cm. To prevent this geometry from being too intrusive, we use an ‘I’ structure, shown in the middle of figure 2. In addition, in this Wheatstone bridge, the two upper (respectively lower) resistors are in the opposite situation (no common point). Since the calibrations of sensors are very close, the output of the bridge is poorly sensitive to the average temperature. But this output is very sensitive to a temperature difference between the top and bottom of the bridge. An Agilent 33220A function generator provides the bridge with a voltage

with a range of 0.1 V and with a frequency of 34 Hz. We measure the output of the bridge with a differential lock-in amplifier (Stanford Research SR8303DSP).

To carry out PIV, we use a one watt green continuous laser (Melles Griot). In a first step, we seed water with hollow glass particles (Sphericul 110P8, LaVision GmbH), 10  $\mu\text{m}$  in average diameter. A laser sheet (DPSS-Laser System, 532 nm, Melles Griot) is created, thanks to a cylindrical lens. We record images of the channel with the Imager Pro Lavisision camera. All our PIV measurements are made at a frequency of 25 Hz and the recording and batch processing are done with Davis Lavisision's software.

The images are grouped in blocks of 20 (0.8 s for the block). The blocks are separated by 2 min, much larger than the correlation time of velocity (see [1]). A record consists of 160 blocks (which corresponds to 5 h and 20 min). All the records are made at an average temperature of 25  $^{\circ}\text{C}$  ( $Pr = 6$ ), close to the room temperature, to minimize eventual heat leaks.

### 3. Brief overview of thermal results

The output of the bridge gives us all the global information on our system. In the absence of convection (no heat flux), it presents no visible fluctuations, which allows us to precisely measure the zero of our bridge. It also allows us to finely check the eventual heat leaks on our hot chamber, which enhance our precision on the heat flux  $Q$ . The average value of the output gives us the temperature gradient  $\beta$ . We checked that its value is reasonably constant when translating the 'I' structure along the axis of the cell [1]. Assuming a short correlation length for the temperature field (we verified this hypothesis), the rms value of the output gives an amplitude  $\theta$  for the temperature fluctuations. With the ratio between  $\theta$  and  $\beta$ , we can define an 'intrinsic' length

$$L = \theta/\beta. \quad (4)$$

Furthermore, the cut-off frequency of the bridge output power spectrum gives a characteristic time  $\tau$ . We verified that  $L/\tau$  is systematically close to the root mean square (rms) value of the velocity. Thus, the only measure of the bridge output gives us the gradient  $\beta$ , the length  $L$  and thus the Rayleigh number  $Ra$  and the Reynolds number if we define it by

$$Re = \frac{L^2}{\nu\tau}. \quad (5)$$

In [1], it has been shown that all the data, whether of the present cell or of another one with  $d$  twice larger (called 'the previous cell' hereafter), at various Prandtl numbers  $Pr$ , agree with the following laws:

$$Nu = 1.6\sqrt{RaPr}, \quad RePr = 1.3\sqrt{RaPr}. \quad (6)$$

It is worth mentioning that, with our choice for  $L$ , the close similitude between  $Nu$  and  $RePr$  has a simple interpretation. The heat flux  $Q$  can be written as

$$Q = C_p(\langle\langle v_z T \rangle\rangle + \kappa\beta), \quad (7)$$

where  $C_p$  is the heat capacity per unit volume ( $\chi = C_p\kappa$ ).  $\langle\langle \cdot \rangle\rangle$  means averaging both on time and the width of the channel. Then, the Nusselt number

$$\begin{aligned} Nu &= \frac{\langle\langle v_z T \rangle\rangle}{\kappa\beta} + 1 \\ &\simeq C_{vT} \frac{\sqrt{\langle\langle \delta T^2 \rangle\rangle}}{\beta} \frac{\sqrt{\langle\langle v_z^2 \rangle\rangle}}{\kappa} \end{aligned} \quad (8)$$

with

$$C_{vT} = \frac{\langle\langle v_z T \rangle\rangle}{\sqrt{\langle\langle v_z^2 \rangle\rangle} \sqrt{\langle\langle \delta T^2 \rangle\rangle}}, \quad (9)$$

where  $\delta T = T - \langle\langle T \rangle\rangle$  is the difference between the instantaneous temperature  $T$  and its average.  $C_{vT}$  is the correlation coefficient between  $v_z$  and  $T$ .

Considering, as we assume, that  $\theta$ , used in the definition of  $L$  (equation (4)), is proportional to  $\sqrt{\langle\langle \delta T^2 \rangle\rangle}$  and  $U$  to  $\sqrt{\langle\langle v_z^2 \rangle\rangle}$ , we can write

$$Nu \propto C_{vT} RePr. \quad (10)$$

If  $C_{vT}$  is constant, the choice we made for  $L$  ensures similar behaviour between  $Nu$  and  $RePr$ .

In a previous study [1], we used a cell ('the previous cell') with the same channel length as here (20 cm) and a width twice as large. Despite this difference in aspect ratio, the  $Nu$  versus  $Ra$  and  $Re$  versus  $Ra$  were in agreement with equation (6). As noted in [1], the same agreement is found with the salt water experiments [2, 3] and the numerical simulations [5, 6].

In the following, all measurements concern velocities, with no direct measure of  $\beta$  and thus of  $L$ . The only thermal information is the heat power input to the hot plate. It is thus useful to translate  $\beta$  in terms of a velocity squared,

$$g\alpha\beta d^2, \quad (11)$$

which is the square of the free fall velocity, under the buoyancy acceleration, on a length  $d$ . Taking into account that, in the regime we explore,  $L \simeq 0.8d$ , the relation  $Nu = 1.6\sqrt{RaPr}$  gives

$$g\alpha\beta d^2 \simeq \left(\frac{Qdg\alpha}{C_p}\right)^{2/3} = U_t^2, \quad (12)$$

which we take as the definition of our reference velocity  $U_t$ .

#### 4. Mean transverse profiles

In [1], a PIV study was analysed, for two different input powers, in the 'previous cell'. In this section, we report a similar study, systematically performed for four different input powers, in our present cell. The goal is multiple. First, we want to check the expected scalings, both with spatial dimensions and the input power. We also want to check the pertinence of the turbulent viscosity approximation, in the present situation, where the Reynolds number is significantly lower than in [1]. Indeed, we shall see in the next section the importance of this concept of turbulent viscosity for interpreting the relation between temperature and vertical velocity fluctuations.

To correctly analyse the flow through PIV techniques, it is very important to take into account one of its characteristics: it often separates into two columns, one ascending and the other descending.

In most of the pictures, the flow is globally ascending in the left-hand part and descending in the right one, or the opposite. These flows we call  $\Phi$ -flows. Some of the pictures show a flow globally ascending in both parts (remember that we record only a sheet of the flow) or descending. We call this kind of flow  $\Xi$ -flows.  $\Phi$ -flows have a typical mixing layer structure. In order to discuss them, first we have to extract the average profile of the velocity field.

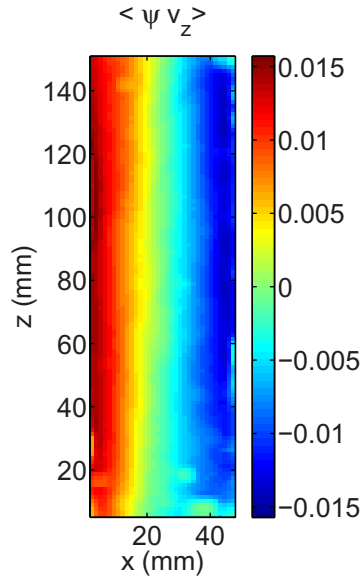


**Figure 3.** Time-averaged values of  $\psi v_z$ .

With this in mind, as done in [1], we first define  $\psi_l$ , which is 1 if the average of the vertical velocity in the left part is positive, and  $\psi_l = -1$  if it is negative. We also define  $\psi_r$ , which is  $-1$  if the average of the vertical velocity in the right part is positive, and  $\psi_r = 1$  if this latter average is negative. For  $\Phi$ -flows,  $\psi_l = \psi_r$ . Reciprocally, for  $\Xi$ -flows,  $\psi_l = -\psi_r$ . We then define

$$\psi = \frac{1}{2}(\psi_l + \psi_r), \quad (13)$$

which is zero for  $\Xi$ -flows and  $\pm 1$  for  $\Phi$ -flows.

Figure 3 shows the average field  $\langle \psi v_z \rangle$ , where  $\langle \cdot \rangle$  stands for time average divided by the time average of  $\psi^2$ , to take into account only the  $\Phi$ -flows.  $\langle \psi v_z \rangle$  presents a reasonable invariance versus  $z$ , as expected for the central part of the channel.

Due to the observed translational invariance, it is reasonable to define the  $z$ -average,

$$U_z(x) = \overline{\langle \psi v_z \rangle}^z, \quad (14)$$

as the profile of the vertical velocity. Here,  $\overline{\langle \cdot \rangle}^z$  stands for a time average, itself averaged along  $z$ . Such profiles are shown in figure 4 for four different applied powers:  $P = 17.3, 45.2, 65.9$  and  $77.9$  W ( $Q = 6920, 18\,100, 26\,400$  and  $31\,200$   $\text{Wm}^{-2}$ ). The same treatment applied to  $v_x$  gives negligible values. In figure 4, in order to increase the statistics, we symmetrize the  $U_z$  profile, i.e. we plot  $(U_z(x) - U_z(d-x))/2$ .

Taking into account these reversals is fundamental for correctly defining fluctuations, and Reynolds stresses, which, in turn, give indirect information about the horizontal temperature profile:

$$\Theta(x) = \overline{\langle \psi T \rangle}^z. \quad (15)$$

As shown in [1],  $\Theta(x)$  and  $U_z(x)$  are related through the differential equation

$$\partial_x(\tau_{xz} - \nu \partial_x U_z) = g\alpha\Theta, \quad (16)$$

where  $\tau_{xz} = \overline{\langle \psi v_x v_z \rangle}^z$  is the transverse Reynolds stress.

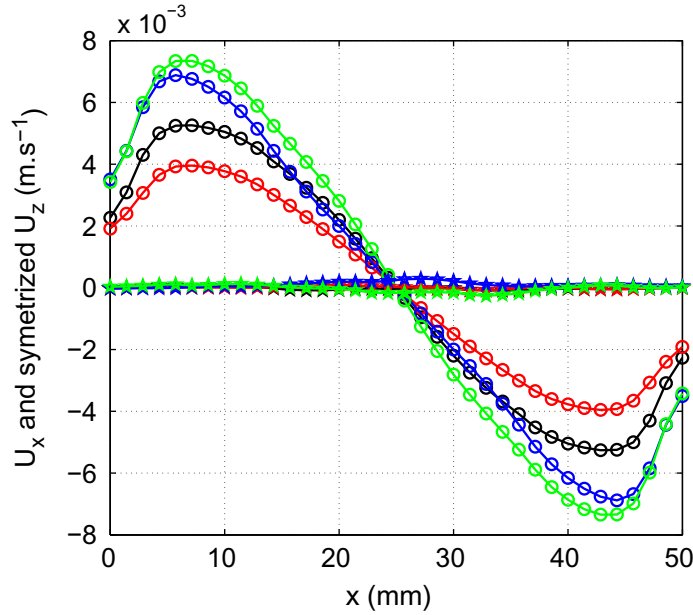


**Figure 4.** Vertical ( $z$ -component, circles) and horizontal ( $x$ -component, stars) velocities, averaged on time and  $z$  for the various applied powers. Red,  $P = 17.3$  W; black,  $P = 45.2$  W; blue,  $P = 65.9$  W; green,  $P = 77.9$  W. The vertical velocity has been symetrized:  $(U_z(x) - U_z(d - x))/2$ . The horizontal velocity is almost zero.

Equation (16) alone shows the importance of  $\tau_{xz}$ , which represents the momentum flux along  $x$  when the viscosity can be neglected. If we forget reversals, this transverse Reynolds stress averages to zero [3].

The two other significant Reynolds stresses,  $\tau_{zz} = \overline{\langle (\psi v_z - \langle \psi v_z \rangle)^2 \rangle^z}$  and  $\tau_{xx} = \overline{\langle (\psi v_x - \langle \psi v_x \rangle)^2 \rangle^z}$ , play little role as stresses, but give a good estimate of the amplitude of the fluctuations. Their profiles are shown in figures 5 and 6, for the same four heat fluxes as above. Note the nice uniformity of  $\tau_{zz}$ . This is not so obvious for  $\tau_{xx}$ , but a constant value approximation remains reasonable. In figures 5 and 6, we do not symmetrize the profiles. The difference between a particular profile and its symmetric gives an estimate of the error bar.

In all the above comments, we dismiss the points very close to the walls for two reasons: the reliability of our PIV measurements is poor here and the viscosity must dominate sufficiently close to the walls.

We turn to the transverse Reynolds stress  $\tau_{xz}$  now. In figure 7, we plot its symmetrized version  $(\tau_{xz}(x) + \tau_{xz}(d - x))/2$ . We remark first that  $\tau_{xz}$  is positive and much larger than the viscous stress  $|\nu \partial_x U_z|$  ( $5 \times 10^{-7} \text{ m}^2 \text{ s}^{-2}$  at the centre for the highest power), except very close to the walls. This means that most of the momentum created by the buoyancy forces directly exchange from one side of the channel to the other, with almost nothing going to the walls. We can practically neglect the friction on the walls. That is why we can compare our experiment to the numerical simulations [5, 6] with periodic boundary conditions.

Secondly, the curvature of the profile is clear. Indeed, this profile is very similar to that of  $dU_z/dx$ , which will allow us to define a turbulent viscosity  $\nu^{\text{turb}}$  through the relation

$$\tau_{xz} = \overline{\langle \psi v_x v_z \rangle^z} = -\nu^{\text{turb}} \frac{dU_z}{dx}. \quad (17)$$

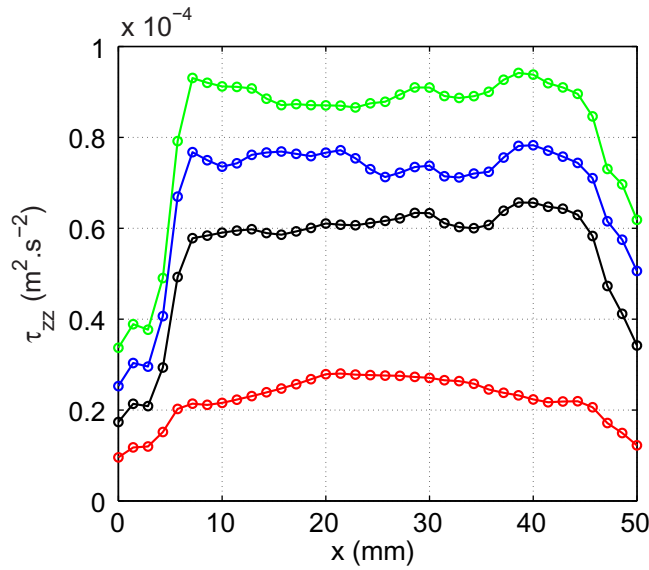


**Figure 5.** Profiles of the vertical velocity fluctuation variance  $\tau_{zz}$  for the four considered applied powers. The same colour code as in figure 4.

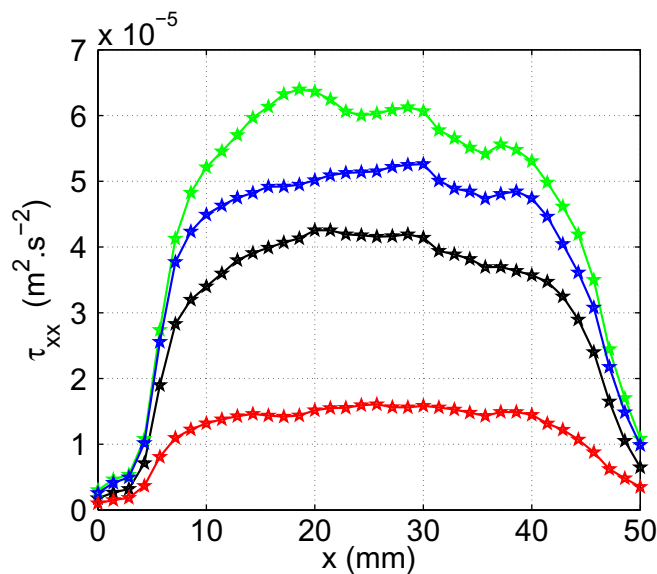


**Figure 6.** Profiles of the horizontal velocity fluctuation variance  $\tau_{xx}$  for the four considered applied powers. The same colour code as in figure 4.

$\tau_{xx}$  and  $\tau_{zz}$  profiles being approximately constant, we can consider this turbulent fluid as homogeneous, with a constant effective viscosity. We can also refer to the cross correlation  $C_{xz}$  between  $v_x$  and  $v_z$ , as shown in figure 8. Note that this cross correlation is independent of the applied power, showing that we are in a high Reynolds inertial limit, despite the relatively low value of our Reynolds number ( $Re = 200-400$ ).

The  $x$  dependence of  $\Theta$  suggests the existence of a horizontal energy flux  $Q_x$ . Again, as shown in [1],  $Q_x$  and  $U_z(x)$  are related through the differential equation

$$C_p \beta U_z = \partial_x Q_x. \quad (18)$$

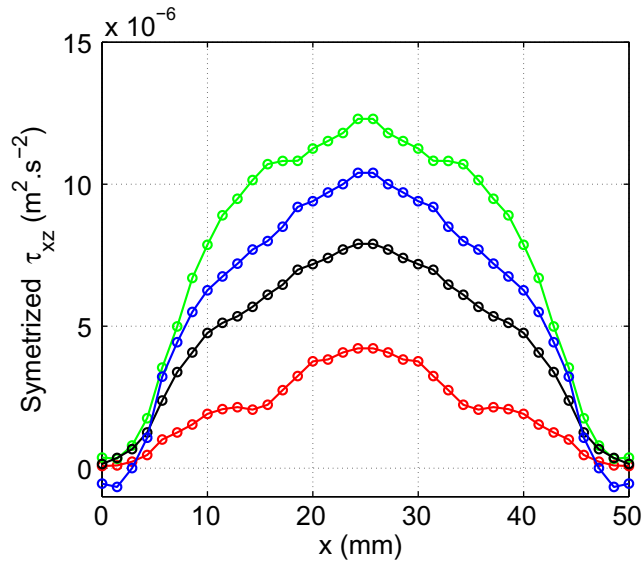


**Figure 7.** The transverse Reynolds  $\tau_{xz}$  stress for the four considered applied powers. Red,  $P = 17.3 \text{ W}$ ; black,  $P = 45.2 \text{ W}$ ; blue,  $P = 65.9 \text{ W}$ ; green,  $P = 77.9 \text{ W}$ . These profiles have been symmetrized:  $(\tau_{xz}(x) + \tau_{xz}(d - x))/2$ . Note its bell shape, while  $\tau_{zz}$  and  $\tau_{xx}$  were much flatter.

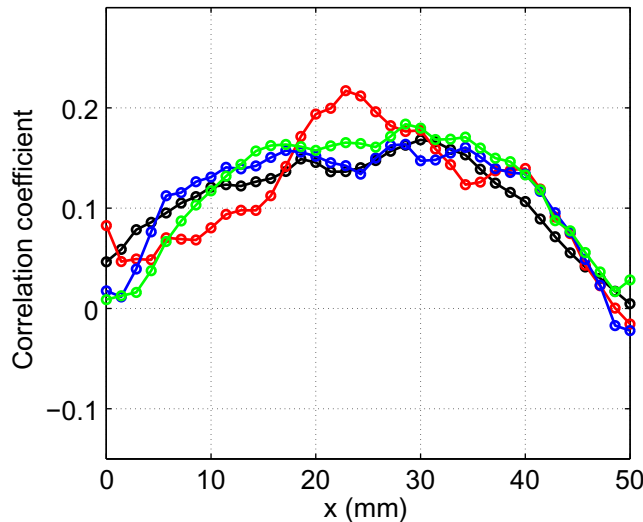


**Figure 8.** Cross-correlation coefficient between  $v_z$  and  $v_x$ . All profiles corresponding to different  $P$  values merge together. Note that the data are not symmetrized here. The colour code is the same as in figure 7.

Thus, measuring  $U_z$  and  $\tau_{xz}$ , we have indirect access to the horizontal heat flux  $Q_x$  and the horizontal temperature profile  $\Theta$ . This allows us to define an effective turbulent heat conductivity  $\chi_x^{\text{turb}}$  through

$$Q_x = -\chi_x^{\text{turb}} \frac{d\Theta}{dx}. \quad (19)$$

However, the noise on averaged quantities forbids calculating derivatives as we have in equations (17)–(19). That is why we smooth the obtained profiles through a simplified model.

We model the major central part of the flow, setting aside two regions  $x < x_-$  and  $x_+ < x$  close to the vertical walls. Considering that the momentum flux toward the walls is very small, a stress-free boundary flow fits the profile of the vertical velocity well:

$$U_z(x) = U_o \cos\left(\pi \frac{x - x_-}{x_+ - x_-}\right). \quad (20)$$

We can then determine  $\nu^{\text{turb}}$  using equation (17), and approximating  $\tau_{xz}(x)$  with a sine function

$$\overline{\langle \psi v_x v_z \rangle^z} = \tau_{xz,o} \sin\left(\pi \frac{x - x_-}{x_+ - x_-}\right) \quad (21)$$

with

$$\tau_{xz,o} = \nu^{\text{turb}} \frac{\pi U_o}{(x_+ - x_-)}. \quad (22)$$

Note that, in order to increase the statistics, we use for these fits the symmetrized profiles:  $(U_z(x) - U_z(d - x))/2$  and  $(\tau_{xz}(x) + \tau_{xz}(d - x))/2$ .

Having  $\nu^{\text{turb}}$ , we can return to equation (16) and determine

$$\begin{aligned} \Theta(x) &= (\nu^{\text{turb}} + \nu) \frac{\pi^2 U_o}{g\alpha(x_+ - x_-)^2} \cos\left(\pi \frac{x - x_-}{x_+ - x_-}\right) \\ &= \Theta_o \cos\left(\pi \frac{x - x_-}{x_+ - x_-}\right). \end{aligned} \quad (23)$$

Finally, using equations (18) and (19), we can determine  $\chi_x^{\text{turb}}$ :

$$\chi_x^{\text{turb}} = C_p \beta \frac{(x_+ - x_-)^4}{\pi^4} \frac{g\alpha}{\nu^{\text{turb}} + \nu}. \quad (24)$$

## 5. Mean flow discussion

We now apply the above discussion to demonstrate the validity of an effective diffusion approach ( $\nu^{\text{turb}}$ ,  $\chi_x^{\text{turb}}$ ) and the inertial scaling of the mean flow. An effective diffusion approach is valid if the mixing length is much smaller than the scale  $d$  of the flow. We can define it in the following way:

$$\nu^{\text{turb}} = L_v \sqrt{\tau_{xx}}, \quad \chi_x^{\text{turb}} = C_p L_{kx} \sqrt{\tau_{xx}}. \quad (25)$$

As we do not measure  $\beta$ , we have to express  $\chi_x^{\text{turb}}$  in terms of  $U_t$ , which is obtained directly from  $P$ . It gives

$$\begin{aligned} \chi_x^{\text{turb}} &= C_p \frac{(x_+ - x_-)^4}{\pi^4} \frac{U_t^2}{\nu^{\text{turb}} d^2} \\ &= C_p \nu^{\text{turb}} \frac{U_o^2 U_t^2 (x_+ - x_-)^2}{\tau_{xz,o}^2 \pi^2 d^2}. \end{aligned} \quad (26)$$

$L_v/d$  and  $L_{kx}/d$  have to be small to give meaning to the effective viscosity and diffusivity coefficient. On the other hand, if the explored range corresponds to a pure inertial behaviour,

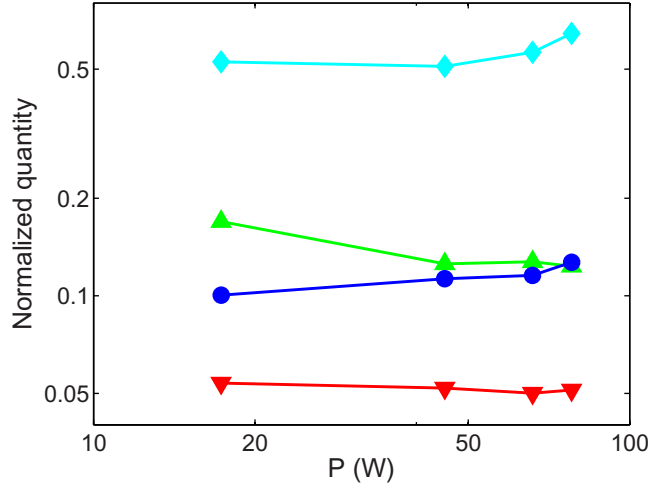


**Figure 9.** The normalized mixing lengths,  $L_v/d$  (triangle down) and  $L_{kx}/d$  (triangle up), the normalized velocity amplitude squared  $\tilde{U}^2$  (diamond) and transverse Reynolds stress  $\tilde{\tau}$  (circle) as a function of  $P$ .

their values have to be independent of the applied power  $P$ . In the same spirit,  $U_t$  must give the velocity scale. We thus expect  $\tilde{U} = U_o/U_t$  and  $\tilde{\tau} = \tau_{xz,o}/U_t^2$  to also be independent of  $P$ .

Figure 9 shows the dependence of  $L_v/d$ ,  $L_{kx}/d$ ,  $\tilde{U}^2$  and  $\tilde{\tau}$  as a function of  $P$ . We give below how these quantities depend on the measured ones:  $U_t$  (equation (12)),  $U_o$  (equation (20) and figure 4),  $\tau_{xz,o}$  (equation (21) and figure 7) and  $\tau_{xx}$  (figure 6):

$$\frac{L_v}{d} = \frac{(x_+ - x_-)}{\pi d} \frac{\tau_{xz,o}}{U_o \sqrt{\tau_{xx}}} \quad (27)$$

$$\frac{L_v}{d} = \frac{(x_+ - x_-)^3}{\pi^3 d^3} \frac{U_o U_t^2}{\tau_{xz,o} \sqrt{\tau_{xx}}}, \quad (28)$$

$$\tilde{U}^2 = \frac{U_o^2}{U_t^2}, \quad (29)$$

$$\tilde{\tau} = \frac{\tau_{xz,o}}{U_t^2}. \quad (30)$$

The values of  $L_v/d$  and  $L_{kx}/d$  are effectively small, and reasonably independent of  $P$ .  $\tilde{U}$  and  $\tilde{\tau}$  are also reasonably independent of  $P$ . We can even define an effective turbulent Prandtl number:

$$Pr^{\text{turb}} = \frac{C_p \nu^{\text{turb}}}{\chi_x^{\text{turb}}} = \frac{\tau_{xz,o}^2}{U_o^2 U_t^2} \frac{\pi^2 d^2}{(x_+ - x_-)^2}. \quad (31)$$

As  $(x_+ - x_-) \simeq d$ ,  $Pr^{\text{turb}} \simeq (\pi \tilde{\tau} / \tilde{U})^2$ . The constant value of  $\tilde{\tau}$  and  $\tilde{U}$  when  $P$  is varied guarantees a constant value for  $Pr^{\text{turb}}$ . This value is close to 0.4. In [1], a value closer to 0.3 was found.

In [1], a careful study of error bars was made, with the conclusion that  $Pr^{\text{turb}}$  is determined within 15%, taking into account its sensitivity to  $(x_+ - x_-)$ . Although at the limit of the error

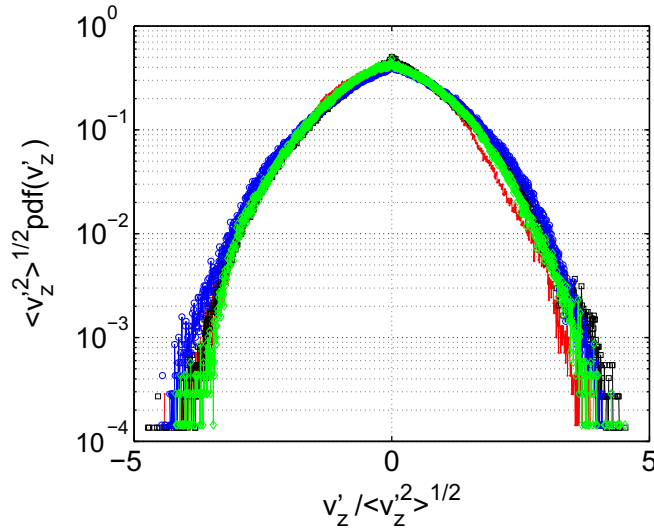


**Figure 10.** Pdfs of the vertical velocity fluctuations, for the different applied powers  $P$ . Once normalized to their rms value, all pdfs merge together.

bar, the difference between 0.3 and 0.4 cannot be considered significant. On the other hand, we confirm that  $Pr^{\text{turb}}$  is significantly smaller than 1 with this flow geometry.

Note that, within the same approximations,  $\Theta_o$  can be written as

$$\Theta_o \simeq \frac{\pi \tau_{xz,o}}{g\alpha(x_+ - x_-)} = \beta d \tilde{\tau} \frac{\pi d}{(x_+ - x_-)}. \quad (32)$$

Again, the constant value of  $\tilde{\tau}$  when  $P$  is varied guarantees a constant value for  $\Theta_o/\beta d$ . The transverse mean temperature gradient is proportional to the vertical one.

## 6. One-point statistics

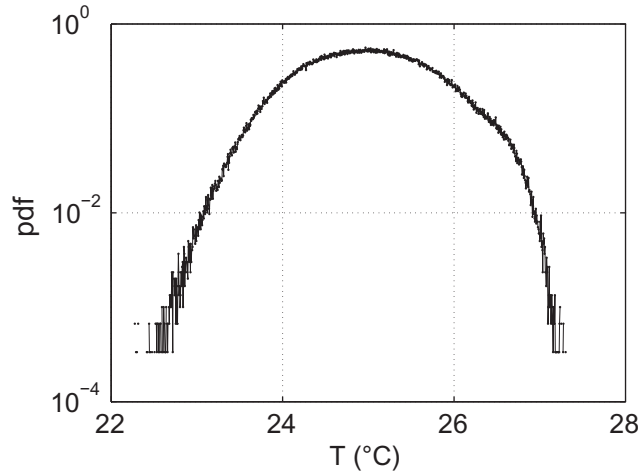
In this section, we examine the one-point statistics of the vertical and horizontal velocity fluctuations, respectively  $v_z'$  and  $v_x'$ . The comparison between them, and with the temperature fluctuations, reveals some apparent contradictions that we shall discuss.

Figure 10 shows the probability density function (pdf) of  $v_z'$ , normalized to its rms, for the four considered input powers. Clearly the shape of these pdfs does not depend on  $P$  and is very close to Gaussian. This is indeed the case in most of the turbulent flows. The surprise comes when comparing to the temperature pdf. The one shown in figure 11 corresponds to  $P = 65.9$  W. Obviously, we cannot distinguish here between  $\psi = 1$  and  $\psi = -1$ , which slightly deforms the pdf. On the other hand, the width of this distribution is much larger than the value of  $\Theta_o$  (0.25 °C here), and the shape of the pdf is close to Gaussian.

This is rather surprising. Looking at the equations, at large scales, the temperature seems to balance with the velocity squared, but a relation like

$$T' = a v_z' \sqrt{v_z'^2} \quad (33)$$

would not be consistent with both  $T'$  and  $v_z'$  being Gaussian.



**Figure 11.** The temperature pdfs for  $P = 65.9$  W, in the middle of the channel. There is no way to correct for the  $\psi$  time dependence here.

This is not due to a small correlation coefficient between  $T'$  and  $v'_z$ , as we will show. Using the values of  $U = 7 \times 10^{-3} \text{ ms}^{-1}$  (see figure 4) and  $\Theta_0 = 0.25 \text{ }^\circ\text{C}$ , the power carried by the mean flow can be estimated as 9 W, which gives 57 W for the fluctuations and

$$\langle v'_z T' \rangle = \frac{57 \text{ W}}{C_p d^2} = 5.5 \times 10^{-3} \text{ K ms}^{-1}. \quad (34)$$

The rms of velocity fluctuations is  $8.5 \times 10^{-3} \text{ ms}^{-1}$  (see figure 5) and that of temperature fluctuations is  $0.75 \text{ }^\circ\text{C}$ . This gives a very large correlation coefficient: 0.86.

This thus leads us to the conclusion that the relation between temperature and vertical velocity is close to linear. This is consistent with the validity of the turbulent viscosity approximation. In this 'viscous turbulent fluid', we can write that velocities are proportional to buoyancy forces,

$$g\alpha T' \simeq v^{\text{turb}} \frac{v'_z}{\ell^2}, \quad (35)$$

$\ell$  being the typical size of large-scale fluctuations. Using the above values, and  $\alpha = 2.57 \times 10^{-4} \text{ K}^{-1}$ , we obtain  $\ell \simeq 1 \text{ cm}$ , close to the mixing length value, which confirms this interpretation.

The pdf of  $v'_x$ , shown in figure 12 for the four applied powers explored, has a shape that differs from the  $v'_z$  one but does not depend on the power  $P$ .

The shape is exponential up to the rms and then approximately Gaussian for the highest absolute values of  $v'_x$ . To interpret this shape, we shall follow the same picture as above, noting that the buoyancy forces have no component along  $x$ . The only driving force, here, is the pressure gradient. Pressure fluctuations  $\delta p$  scale as the velocity fluctuations squared, so we assume a similar distribution for these quantities. We thus write

$$\frac{\delta p}{\ell} \simeq \frac{v_z^2}{\ell} \simeq v^{\text{turb}} \frac{v'_x}{\ell^2}. \quad (36)$$

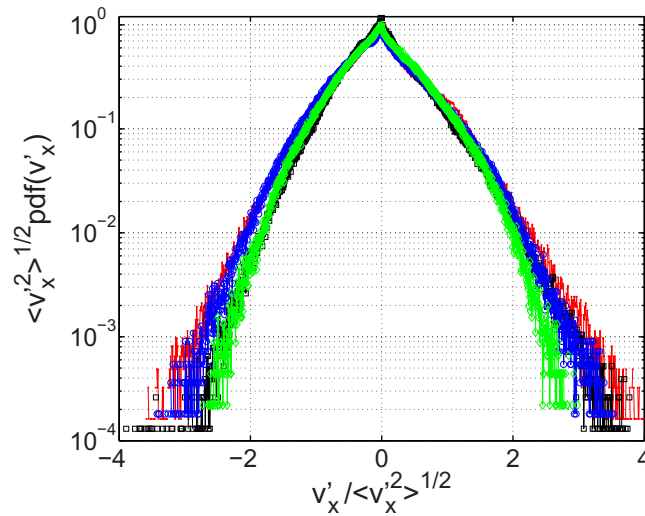


**Figure 12.** Pdfs of horizontal velocity fluctuations, normalized to their rms values. Note the exponential shape for small amplitudes.

This gives

$$v_x' \simeq \frac{v_z'^2 \ell}{\nu_{\text{turb}}}, \quad (37)$$

which explains why  $v_x'$  behaves as  $v_z'^2$  while its variance scales as the  $v_z'$  one.

To conclude this section, we note that assuming the fluctuations follow the macroscopic rules, as is generally admitted in statistical physics, well explains the respective shapes of temperature,  $v_z'$  and  $v_x'$  pdfs.

## 7. Two-point statistics

This section is devoted to the study of two-point correlations through the statistics of velocity differences,

$$\delta_i v_j = v_j(x_i + a) - v_j(x_i), \quad (38)$$

where  $i = x, z$  indicates the orientation of the vector joining the two points (e.g.  $x_z = z$ ) and  $j = x, z$  indicates the velocity component whose difference is taken.

For instance, figure 13 shows the pdfs of the vertical velocity component differences on various vertical distances.

Several remarks can be made. Firstly, these pdfs have a clear dissymmetry (skewness), the negative wing being fatter than the positive one. As we are considering longitudinal differences, this feature is similar to what occurs in isotropic turbulence. Secondly, the shape of the pdfs changes with distance. Again, this corresponds to intermittency in isotropic turbulent flows. Finally, the obvious change in width can be characterized by the second-order structure function,  $\langle (\delta_z v_z)^2 \rangle(a)$ . This is shown, for each applied power, in figure 14.

Let us begin with the skewness. If we have time-reversal symmetry for the problem at hand, the skewness would be zero. The dissipated power per unit mass,  $\epsilon$ , which breaks the

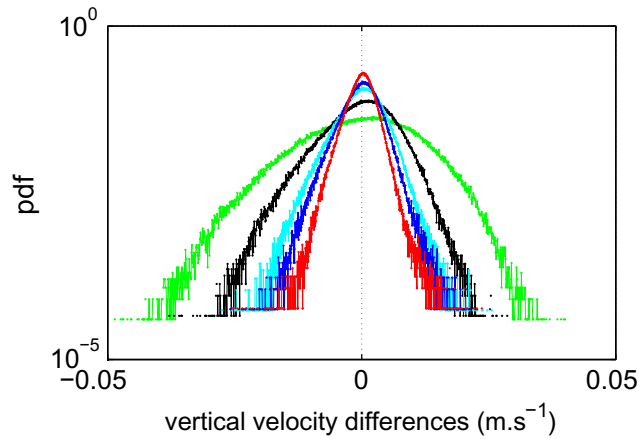


**Figure 13.** Pdfs of vertical velocity differences  $v_z(z+a) - v_z(z)$ , for  $a = 2.4$  (red), 3.7 (blue), 4.9 (cyan), 9.9 (black) and 34.5 mm (green).

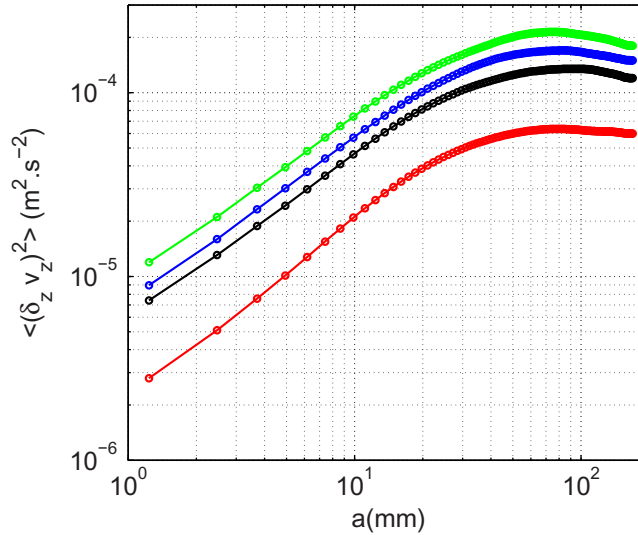


**Figure 14.** The second-order structure function  $\langle (\delta_z v_z)^2 \rangle$  of vertical velocity differences, for the various  $P$  values: red,  $P = 17.3$  W; black,  $P = 45.2$  W; blue,  $P = 65.9$  W; green,  $P = 77.9$  W.

time-reversal symmetry, should thus be proportional to the third-order moment,  $\langle (\delta_z v_z)^3 \rangle$ , as in isotropic turbulence. Here,  $\epsilon$  can easily be related to the applied power  $P$  or to the heat flux  $Q$ :

$$\epsilon = g\alpha \langle T v_z \rangle = \frac{g\alpha Q}{C_p} = \frac{U_t^3}{d}. \quad (39)$$

Figure 15 shows  $\langle (\delta_z v_z)^3 \rangle / U_t^3$  as a function of the vertical distance  $a$ .

The four sets of values nicely merge, particularly for small  $a$ . However, even on this linear plot, it is clear that this quantity is not proportional to  $a$ , as it should be within a true inertial range, far from both dissipation and the large scale  $d$ . A calculation of the orders of magnitude will explain why.

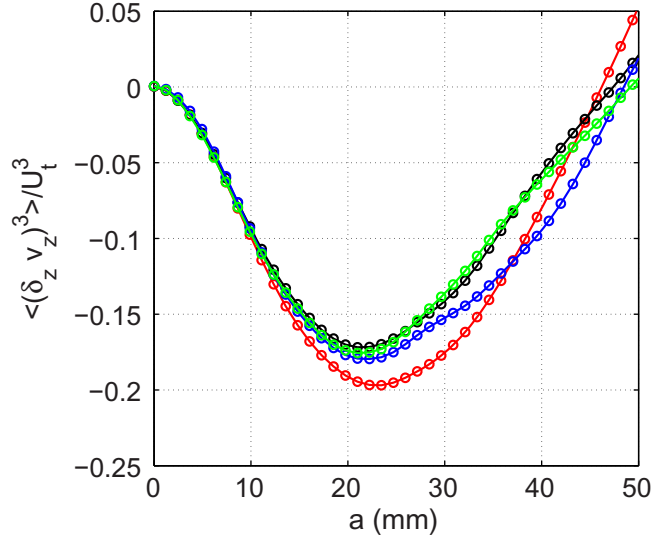


**Figure 15.** The normalized third moment  $\langle (\delta_z v_z)^3 \rangle / U_t^3$  versus the vertical distance  $a$ . The same colour code as in figure 14.

Two lengths are important in developed turbulence: the dissipative length  $\eta$  and the Taylor length  $\lambda$ .

$$\eta^4 = \frac{v^3}{\epsilon} = \frac{v^3 C_p}{g\alpha Q}. \quad (40)$$

Thus  $\eta$  is inversely proportional to  $P^{1/4}$  ( $P = Qd^2$ ). In our system,

$$\eta \simeq 1.4 \times 10^{-3} P^{-1/4}, \quad (41)$$

with  $P$  in watts and  $\eta$  in metres. It gives a fraction of millimetre in our experiments, which is smaller than our resolution, which explains why we do not observe the trivial viscous scaling  $\langle (\delta_z v_z)^p \rangle \propto a^p$ , even for the lowest values of  $a$ .

$$\lambda^2 = 15v \frac{\langle v'^2 \rangle}{\epsilon} = 15v \frac{\langle v'^2 \rangle C_p}{g\alpha Q}, \quad (42)$$

where the factor 15 refers to the isotropic case, as we aim at an order of magnitude. As  $\langle v'^2 \rangle$  is proportional to  $P^{2/3}$ , we see that  $\lambda$  is inversely proportional to  $P^{1/6}$  and

$$\lambda \simeq 1.7 \times 10^{-2} P^{-1/6}, \quad (43)$$

with  $P$  in watts and  $\lambda$  in metres, so that  $\lambda$  is about 1 cm in our experiments.  $\lambda$  can be used to define a Reynolds number  $R_\lambda$ :

$$R_\lambda^2 = 15 \frac{\langle v'^2 \rangle^2}{\epsilon v} = 15 \frac{\langle v'^2 \rangle^2 C_p}{v g \alpha Q}. \quad (44)$$

In our experiments,  $R_\lambda \simeq 10P^{1/6}$ , with  $P$  in watts. For the maximum value of  $P$ , it gives 21. This value is too small for developing a true inertial range.

Intermittency, even at such small  $R_\lambda$ , can be revealed by quantities like

$$F_3 = \frac{\langle |\delta_z v_z|^3 \rangle}{\langle |\delta_z v_z| \rangle^3}. \quad (45)$$

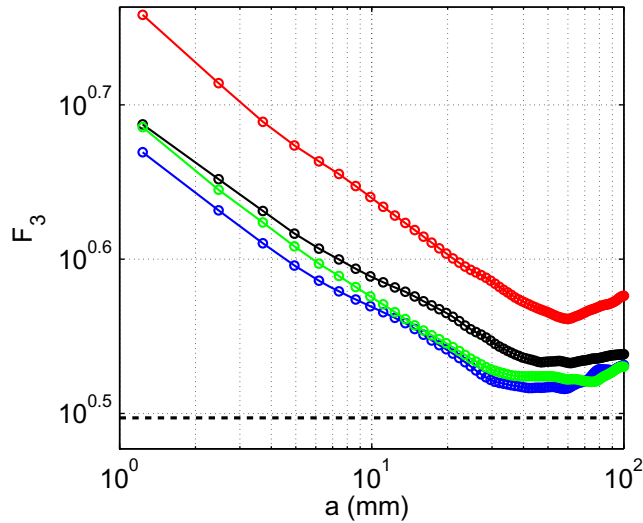


**Figure 16.** The ‘flatness’  $F_3 = \langle |\delta_z v_z|^3 \rangle / \langle |\delta_z v_z| \rangle^3$  for the various  $P$  values. Red,  $P = 17.3$  W; black,  $P = 45.2$  W; blue,  $P = 65.9$  W; green,  $P = 77.9$  W. A Gaussian distribution gives  $F_3 = \pi$  (dashed line).

This is a kind of flatness due to the use of absolute values and it avoids calculating  $\langle (\delta_z v_z)^4 \rangle$ , which would ask for very high statistics. Such a quantity is expected [9] to be constant both at large and small scales, and to have an inertial range (a power law in  $a$ ) and an intermediate dissipative range (a rather rapid drop between dissipative and inertial scales) behaviours. The transition between large and inertial scales is neat (see figure 16), giving 3.5 cm for the scale  $a$  under which the cascade of energy develops. Again, due to our small  $R_\lambda$  values, there is no true power law behaviour. The value of  $F_3$  for a Gaussian distribution is  $\pi$ . Indeed, it slightly differs from  $\pi$  at large scales, particularly for the lowest  $P$  value, revealing small differences with the Gaussian shape.

We also looked at differences of  $v'_x$  along  $z$  (transverse differences), as well as those of  $v'_x$  and  $v'_z$  along  $x$ . Would the turbulence be isotropic, the transverse second-order structure functions, both in the  $x$ - and  $z$ -directions, would be identical, the same for longitudinal ones. However, a difference would appear between transverse and longitudinal structure functions. This is why we separately plot the transverse second-order structure functions (in figure 17) and the longitudinal ones (in figure 18), normalized by  $U_t^2$ . They have the usual behaviour, the transverse ones seemingly shifted toward the small  $a$  values compared with the longitudinal ones (see, for instance, [10]). Here, the characteristic lengths are smaller in the  $x$  (horizontal) direction than in the  $z$  (vertical) one, due to the anisotropy.

We have to stress the behaviour of the second-order structure function of the  $x$  velocity component both transverse and longitudinal, for the smallest  $P$  value, as it clearly does not merge with others. The same difference with the other powers, contrary to the  $v_z$  case, appears when considering  $\langle (\delta_x v_x)^3 \rangle / U_t^3$  (figure 19).

The interesting point is that the problem cannot be solved by a simple change in  $U_t$ ; thus it is not due to a bad evaluation of the heat flux or of velocities. This could reveal a transition, at low  $Ra$  number, but further investigation will be necessary to confirm or deny this hypothesis.

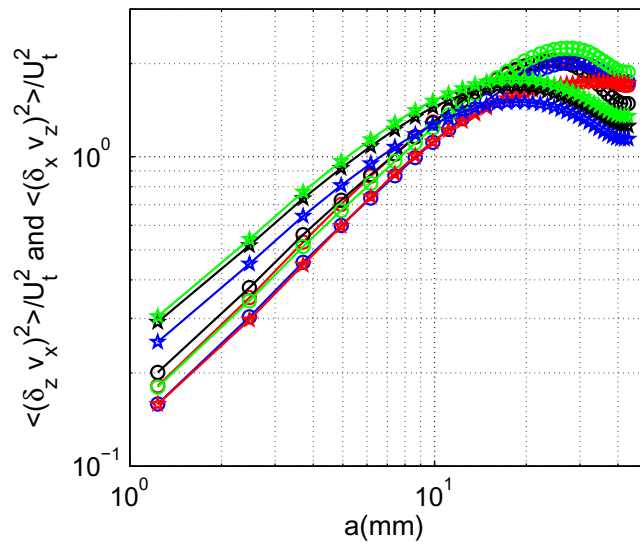


**Figure 17.** The transverse second-order structure functions, normalized with  $U_t^2$ , versus the distance  $a$  in the vertical ( $\langle (\delta_z v_x)^2 \rangle / U_t^2$ ,  $\circ$ ) and horizontal ( $\langle (\delta_x v_z)^2 \rangle / U_t^2$ ,  $\star$ ) directions. The same colour code as in figure 16.

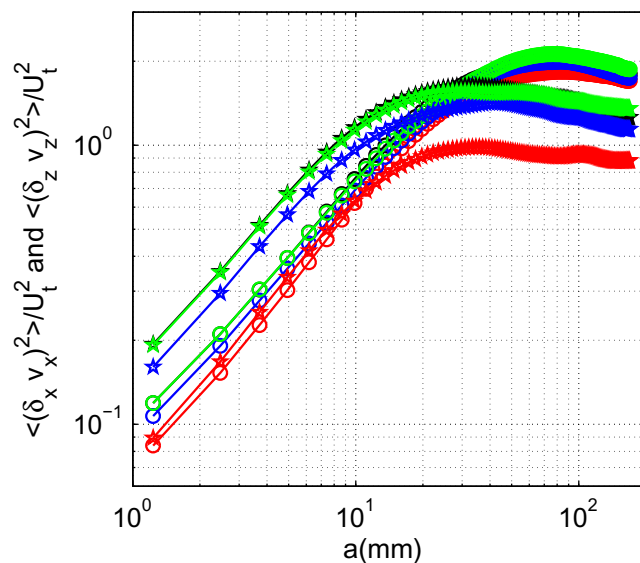


**Figure 18.** The longitudinal second-order structure functions, normalized with  $U_t^2$ , versus the distance  $a$  in the vertical ( $\langle (\delta_z v_z)^2 \rangle / U_t^2$ ,  $\circ$ ) and horizontal ( $\langle (\delta_x v_x)^2 \rangle / U_t^2$ ,  $\star$ ) directions. The same color code as in figure 16.

## 8. Conclusions

This study of the velocity field for the heat convection in a vertical channel completes the works [1, 7], mainly based on thermal measurements. The relative independence versus the applied power  $P$  of all the normalized functions and profiles confirms the inertial character of the mechanisms involved: the molecular viscosity and the molecular diffusivity have a poor

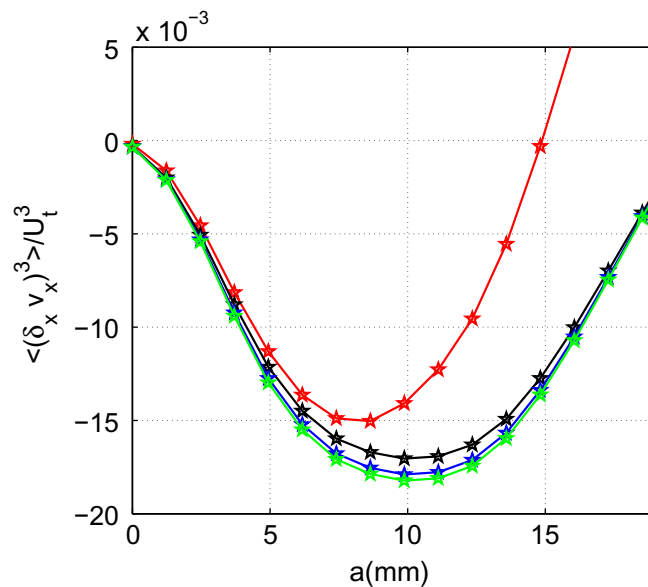


**Figure 19.** The normalized third moment  $\langle (\delta_x v_x)^3 \rangle / U_t^3$  versus the horizontal distance  $a$ . The same colour code as in figure 16.

influence in the explored range. On the other hand, the study of small scales shows that the energy cascade is not well developed, even if some intermittency is present. It leads to the conclusion that the transition observed in [1], where the characteristic length  $L$  begins to depend on the Reynolds number  $Re$ , should coincide with the apparition of an inertial range. The regime explored here could be called ‘intermediate turbulence’.

In this ‘intermediate turbulent’ state, the notions of turbulent viscosity and turbulent diffusivity appear meaningful and powerful. They can be invoked even for the relation between the various fluctuation fields, temperature and both velocity components. We find here a situation reminiscent of solid state statistical physics. It results in well-defined quantities, as mixing lengths or turbulent Prandtl numbers, whose determination from first principles is a challenge for future studies.

### Acknowledgments

We are indebted to the whole team of the collaboration GIMIC for their visits and numerous enlightening discussions. Thanks are also due to F Dumas, F Vittoz and M Moulin for technical assistance. This work was supported by the Agence Nationale pour la Recherche under contract no. ANR-07-BLAN-0181.

### References

- [1] Gibert M, Pabiou H, Tisserand J-C, Gertjerenken B, Castaing B and Chillà F 2009 Heat convection in a vertical channel: plumes versus turbulent diffusion, *Phys. Fluids* **21** 035109
- [2] Cholemani M R and Arakeri J H 2005 Experiments and a model of turbulent exchange flow in a vertical pipe *Int. J. Heat Mass Transfer* **48** 4467–73

- [3] Cholemani M R and Arakeri J H 2009 Axially homogeneous, zero mean flow buoyancy-driven turbulence in a vertical pipe *J. Fluid Mech.* **621** 69–102
- [4] Znaïen J, Hallez Y, Moisy F, Magnaudet J, Hulin J P, Salin D and Hinch E J 2009 Experimental and numerical investigation of flow structures and momentum transport in a turbulent buoyancy driven flow inside a tilted tube *Phys. Fluids* **21** 115102
- [5] Calzavarini E, Lohse D, Toschi F and Tripicciono R 2005 Rayleigh and Prandtl number scaling in the bulk of Rayleigh–Bénard turbulence *Phys. Fluids* **17** 055107
- [6] Lohse D and Toschi F 2003 Ultimate state of thermal convection *Phys. Rev. Lett.* **90** 034502
- [7] Gibert M, Pabiou H, Chillà F and Castaing B 2006 High-Rayleigh-number convection in a vertical channel *Phys. Rev. Lett.* **96** 084501
- [8] Lohse D and Xia K Q 2010 Small-scale properties of turbulent Rayleigh–Benard convection *Annu. Rev. Fluid Mech.* **42** 335–64
- [9] Chevillard L, Castaing B and Lévêque E 2005 On the rapid increase of intermittency in the near-dissipation range of fully developed turbulence *Eur. Phys. J. B* **45** 561–7
- [10] Malécot Y, Auriault C, Kahalerras H, Gagne Y, Chanal O, Chabaud B and Castaing B 2000 A statistical estimator of turbulence intermittency in physical and numerical experiments *Eur. Phys. J. B* **16** 549